Available online at www.sciencedirect.com
ScienceDirect
Cement and Concrete Research 36 (2006) 1548–1555
Cement and Concrete Research

Analysis of CCRL proficiency cements 151 and 152 using the Virtual Cement and Concrete Testing Laboratory

Jeffrey W. Bullard *, Paul E. Stutzman

Materials and Construction Research Division, National Institute of Standards and Technology, Gaithersburg, Maryland, 20899-8615, USA

Received 20 October 2005; accepted 30 May 2006

Abstract

To test the ability of the Virtual Cement and Concrete Testing Laboratory (VCCTL) software to predict cement hydration properties, characterization of mineralogy and phase distribution is necessary. Compositional and textural characteristics of Cement and Concrete Reference Laboratory (CCRL) cements 151 and 152 were determined via scanning electron microscopy (SEM) analysis followed by computer modeling of hydration properties. The general procedure to evaluate a cement is as follows: (1) two-dimensional SEM backscattered electron and X-ray microanalysis images of the cement are obtained, along with a measured particle size distribution (PSD); (2) based on analysis of these images and the measured PSD, three-dimensional microstructures of various water-to-cement ratios are created and hydrated using VCCTL, and (3) the model predictions for degree of hydration under saturated conditions, heat of hydration (ASTM C186), setting time (ASTM C191), and strength development of mortar cubes (ASTM C109) are compared to experimental measurements either performed at NIST or at the participating CCRL proficiency sample evaluation laboratories. For both cements, generally good agreement is observed between the model predictions and the experimental data.
Published by Elsevier Ltd.

Keywords: Building technology; Computer modeling; Cement; Heat of hydration; Hydration kinetics; Particle size distribution; SEM imaging; Strength development

1. Introduction

Improvements in materials characterization should lead to improved performance prediction. Cement characterization by scanning electron microscopy (SEM) provides mineralogical and textural information for hydraulic cements [1]. The Cement and Concrete Reference Laboratory (CCRL), located at the National Institute of Standards and Technology (NIST), biannually issues pairs of proficiency samples of portland cement to be evaluated by hundreds of testing laboratories using ASTM standard test methods [2]. The chemical characteristics and performance properties of these cements are therefore extremely well documented [3], making them ideal systems against which to gauge the predictive capability of the NIST Virtual Cement and Concrete Testing Laboratory computer models [4]. The key module of VCCTL used in this study is a collection of programs for creating and simulating the hydration of three-dimensional microstructures, which is based on the NIST microstructure and hydration model CEMHYD3D [5,6]. Five years ago, a comparison of predictions made by these models was performed using CCRL proficiency samples 135 and 136, with respect to hydration kinetics, heat of hydration, and mortar strength development [7]. At that time, good agreement was observed between model predictions and experimental measurements of these properties.

Over the past five years numerous extensions of the computer model have been made. Foremost among these changes are (1) the ability to estimate the pH of the capillary pore solution of a cement paste and to make the kinetics of hydration dependent upon pH, and (2) incorporation of additional solid phases into the model, especially potassium sulfate, sodium sulfate, and free lime. In addition, adjustments have been made to model parameters in an effort to better predict the behavior of a wider range of cements than those upon which the model was originally calibrated. Therefore, it seems desirable to conduct another study of the predictive capability of the newest version of VCCTL against two more recent CCRL proficiency samples.

SEM images and quantitative phase analysis results for CCRL cements 151 and 152 will be compared to the potential

* Corresponding author.
E-mail address: jeffrey.bullard@nist.gov (J.W. Bullard).

0008-8846/$ - see front matter. Published by Elsevier Ltd.
doi:10.1016/j.cemconres.2006.05.024

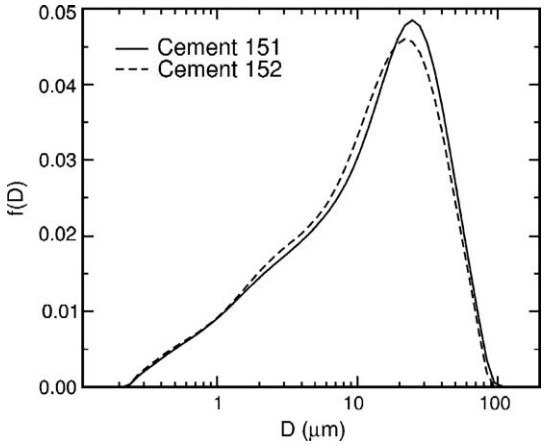

Fig. 1. Particle size distributions, plotted as probability density functions, measured for CCRL cements 151 and 152 using laser diffraction from a dilute suspension of particles in isopropyl alcohol.

phase composition determined via ASTM C150 [2]. Additionally, VCCTL and supplemental experimental measurements will be applied to predicting the hydration kinetics, heat of hydration, and mortar strength development of the two cements. The latter two properties are compared to those measured by CCRL proficiency sample evaluation laboratories, while the hydration kinetics are compared to estimates of the degree of hydration made from loss-on-ignition measurements or from continuous thermogravimetric analysis (TGA) [8].

2. Experimental procedure

2.1. Particle size distribution

The particle size distributions (PSDs) of CCRL cements 151 and 152 were determined using laser diffraction through a dilute suspension of cement particles in isopropyl alcohol. The average particle size distributions for both cement samples are plotted as probability density functions in Fig. 1. The measured PSDs of the two cements are quite similar to each other; in fact, neither the mean particle diameter nor the median particle diameter, on a volume basis, differ by more than 1.0 μm between the two cements. The mean Blaine finenesses reported for cements 151 and 152 are 379 m^2/kg and 409 m^2/kg, respectively, as measured according to ASTM C204 [2] in the CCRL testing program [3]. The difference is consistent with the data in Fig. 1 showing cement 152 to be slightly finer than cement 151.

2.2. Microstructure imaging and segmentation

The preparation techniques for specimens analyzed by SEM and X-ray microanalysis have been described in detail elsewhere [9,1], so only a brief description will be provided here. Polished specimens are made by blending approximately 25 g of cement powder with an epoxy resin to form a viscous paste. The mixture is pressed into a cylindrical mold (3.2 cm diameter) and cured at 60 °C for 24 h. The cured specimen is then cut to obtain a plane surface for imaging. The resulting saw marks are removed by grinding with 400 grit sandpaper, followed by a finer grinding with 600 grit sandpaper. Final polishing is performed on a lap wheel with (6, 3, 1, and 0.25) diamond paste for about 90 s each. After each polishing, the specimen is cleaned with a cloth. After the final polishing step, the specimen is coated with carbon to provide a conductive surface.

The polished specimen is placed in the SEM chamber, and both backscattered electrons (BE) and X-rays (XR) are collected. Typical accelerating voltage and probe current for the backscattered electron images are 10 kV and 2 nA, respectively. X-ray element images are collected for Ca, Si, Al, Fe, S, K, Na, and Mg simultaneously with the BE image, so they can be superimposed to form a composite image of the microstructure with element-specific information at each pixel. A backscattered electron image of cement 151 is shown in Fig. 2. The combined X-ray element maps for a given image field were used to determine the distribution of mineral phases by traversing a decision tree for each pixel in the image. The decision tree is shown as a flow chart in Fig. 3.

After the decision tree is applied, pixel-by-pixel, the resulting segmented image still contains a substantial amount of random noise carried over from the noise of the X-ray element maps. The image quality is improved by sequentially filtering the segmented image through three noise-reducing algorithms. In the first algorithm, all isolated solid pixels surrounded by void space are converted to void space. The second algorithm converts isolated void space that is surrounded by solids to the majority solid phase of the neighboring pixels. The third algorithm is a median filter [10], which replaces each solid pixel by the majority solid phase in the surrounding neighborhood, which typically is taken to be a 5 × 5-pixel square centered on the pixel in question.

An example of the segmented image of cement 151, following the noise filtering procedure just described, is shown in Fig. 4. Seven separate image fields for cement 151 and six separate image fields for cement 152 were acquired and segmented as described in this section.

2.3. Stereological analysis

The cement images were analyzed quantitatively to determine properties of interest for modeling the 3-D microstructure

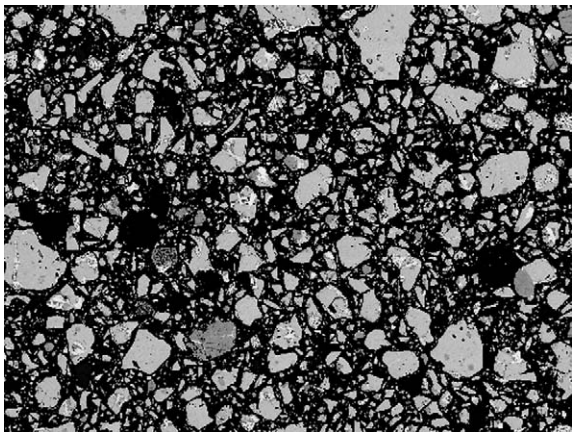

Fig. 2. Backscattered electron image of cement 151. Black regions are epoxy-filled pore space. The image field dimensions are 256 μm × 200 μm.

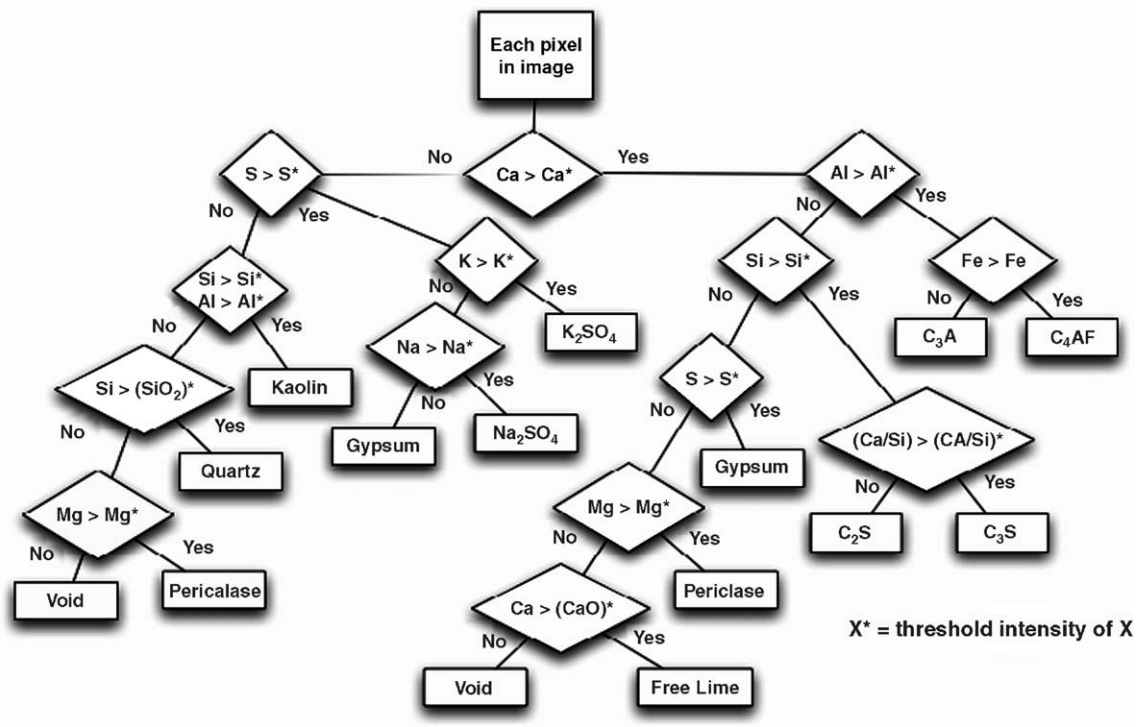

Fig. 3. Decision tree for pixel-by-pixel segmentation of a cement image into its mineral components. Conventional cement chemistry notation is used: C_3S denotes tricalcium silicate, C_2S denotes dicalcium silicate, C_3A denotes tricalcium aluminate, and C_4AF denotes tetracalcium aluminoferrite. Adapted from [1].

and hydration; (1) the area fraction, (2) the surface perimeter fraction of the mineral phases, and (3) their spatial distribution. The volume fraction of each phase determines the extent of each hydration reaction that can occur, and the surface area fraction of each phase influences the rate at which dissolution of that phase into the adjacent water-filled porosity can proceed. Assuming that the microstructure is isotropic, the area fraction of each phase in the 2-D image will equal its volume fraction in a 3-D microstructure. Similarly, the surface perimeter fraction in 2-D will equal the surface area fraction in 3-D. Simple pixel counting and examination of the neighborhood surrounding each pixel are used to determine the 2-D area fraction and surface perimeter fraction of phases in images like those in Fig. 4.

The spatial distribution of clinker phases in the microstructure is quantified by calculating the two-point correlation functions on the images. On an $M \times N$ digital image field, the two-point correlation function, $S_p(x, y)$, for any phase p is given by:

$$S_p(x,y) = \sum_{i=1}^{M-x}\sum_{j=1}^{N-y}\frac{I_p(i,j)\cdot I_p(i+x,y+j)}{(M-x)(N-y)} \quad \begin{matrix} 1 \le x \le M \\ 1 \le y \le N \end{matrix} \qquad (1)$$

where $I_p(x, y)=1$ if the pixel at location (x, y) contains the phase or phases designated by p, and $I_p(x, y)=0$ otherwise. Again assuming that the microstructure is isotropic, $S_p(x, y)$ may be transformed to a function of distance only, $S_p(r)$, where $r = \sqrt{x^2 + y^2}$. Correlation functions for isotropic materials are identical in 2-D and 3-D, so the correlation functions calculated on the final images in Fig. 4 can be used directly to reconstruct 3-D microstructures with the same statistical spatial distribution of phases. The value of $S_p(0)$ is equal to the area fraction of phase p in the image, and the surface perimeter L_p per unit area A_p of phase p is given by the expression

$$\frac{L_p}{A_p} = -4\frac{dS_p(r)}{d_r}|_{r=0} \qquad (2)$$

In other words, knowledge of $S_p(r)$ for each phase of interest is sufficient to reconstruct a 3-D microstructure from the 2-D image.

For both cements 151 and 152, the compositions averaged from the collection of final cement images have been compared to estimates made both by bulk quantitative X-ray diffraction

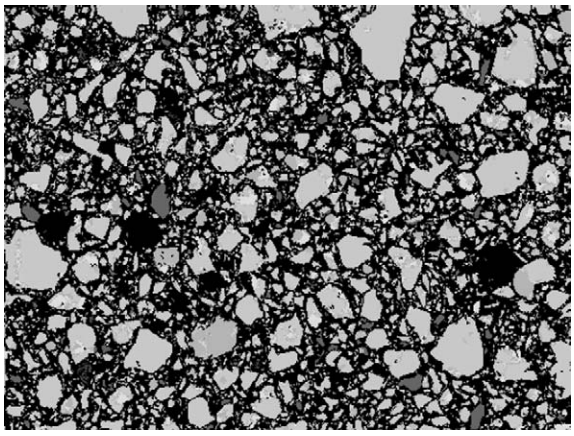

Fig. 4. Final processed image of cement 151. The phases shown, in decreasing order of brightness, are periclase, ferrite, alite, belite, alkali sulfates, aluminate, gypsum, quartz, and calcite. The image field dimensions are 256 μm × 200 μm.

(QXRD) and by cement oxide composition using ASTM C150 [2]. The estimates are shown in Table 1 for cement 151 and in Table 2 for cement 152.

The detection of K_2SO_4, and Na_2SO_4 is difficult using SEM/X-ray microanalysis because the quantities are so small and usually appear in very small domains within the cement. Therefore, ion chromatography (IC) was used to estimate the readily soluble alkali oxide content in both cements. Pastes were allowed to cure for 1 h, after which the capillary pore solution was extracted by centrifuging the specimens for 5 min. A diluted sample of the pore solution was analyzed for Na^+ and K^+ cations (Table 3).

2.4. Estimating degree of hydration

The degree of hydration of paste specimens was estimated by measurement of the loss on ignition (LOI), defined as the average difference between the measured masses at 105 °C and 1000 °C, of the paste. LOI measurements were made after hydration of 3 h, 6 h, 12 h, 24 h, 48 h, 169 h (7 d), 336 h (14 d), 672 h (28 d), or 1344 h (56 d). This experimental technique is similar to that used to measure the non-evaporable water content of a cement paste [10], except that the latter procedure uses D-drying instead of the 105 °C heat treatment.

Two different atmospheres were used in the ovens. The first ('normal') consisted of static ambient laboratory air with a dew point of about 13 °C and CO_2 content of approximately 50 μPa/Pa (50 ppm). The other atmosphere ('dry') consisted of slowly flowing air (about 4 cm^3/min) with a dew point of about −70 °C and a CO_2 content of less than 1 μPa/Pa (1 ppm).

To convert LOI measurements to estimated degree of hydration, it is necessary to measure the LOI of a specimen that has been fully hydrated (Table 4). Also included in the table for comparison is an estimate of the LOI at full hydration based on quantitative X-ray diffraction of the initial powders. The degree of hydration for all the pastes was then estimated by dividing the LOI of the paste by the LOI of the fully hydrated paste. Note that the experimentally measured LOI at full hydration is significantly higher than that estimated from bulk composition.

2.5. Thermogravimetry

Continuous thermogravimetric analysis (TGA) was undertaken on certain pastes cured to different ages to determine the major sources of mass loss between 105 °C and 1000 °C. For this type of measurement, a specimen was equilibrated at 105 °C for 20 h to 24 h in either the normal or dry environments, as described in the previous section. Following this treatment, the specimen was transferred to the TGA apparatus and heated at 5 °C/min to 1000 °C in a N_2 atmosphere. Temperature and mass data were recorded about once every 6 s.

Table 1
Comparison of estimated volume fractions of the four major clinker phases in cement 151, made by SEM image segmentation, quantitative X-ray diffraction (QXRD), and ASTM C150

Phase	SEM	SEM-perimeter	QXRD	ASTM C150
Alite	62.2±3.9[1]	55.6±4.6	63.8	70.9±4.3[2]
Belite	19.1±3.6	26.0±5.7	13.0	9.7±3.8
Aluminate	4.4±2.3	5.9±2.9	4.7	7.9±0.5
Ferrite	14.3±2.3	12.5±2.1	11.8	11.6±0.2

All quantities are expressed on a mass percent basis.
[1]Uncertainty expressed as ± one standard deviation calculated from a sample of seven images.
[2]Uncertainty expressed as ± one standard deviation calculated from over 150 values.

Table 2
Comparison of estimated volume fractions of the four major clinker phases in cement 152, made by SEM image segmentation, quantitative X-ray diffraction (QXRD), and ASTM C150

Phase	SEM	SEM-perimeter	QXRD	ASTM C150
Alite	73.3±0.8[1]	68.7±2.1	63.6	61.5±4.5[2]
Belite	9.6±0.6	13.4±1.2	14.9	10.8±4.0
Aluminate	12.4±0.8	13.9±1.2	14.4	11.0±0.5
Ferrite	4.7±0.4	4.1±0.5	9.7	7.3±0.2

All quantities are expressed on a mass percent basis.
[1]Uncertainty expressed as ± one standard deviation calculated from a sample of six images.
[2]Uncertainty expressed as ± one standard deviation calculated from over 150 values.

3. Results

3.1. Hydration kinetics

The heat of hydration was determined by the testing laboratories using the ASTM C186 heat of solution test method [2]. To predict these values using VCCTL, hydration of a w/c = 0.4 cement paste under sealed conditions at 23 °C was conducted for cements 151 and 152. In Fig. 5, the simulated heats of hydration of both cements as a function of time is compared with the average values measured by the testing laboratories at 7 d and at 28 d. The values of the time conversion factor used for the predicted curves shown in the figure are $\beta = 0.00020$ h/cycle^2 and 0.00057 h/cycle^2 for cements 151 and 152, respectively. These values were chosen to give the best fit to the experimental data in the plot, and these same values will be used throughout the remainder of the paper. In each case the predictions fit the measurements obtained by the testing laboratories quite well at both ages.

Fig. 6 shows plots of the model predictions and experimental results for degree of hydration for cement 151 at w/c = 0.35 and w/c = 0.45. The same value of $\beta = 0.00020$ h/cycle^2 was used as in Fig. 5. The match between prediction and experiment is not as good at either w/c ratio as it is in Fig. 5. Adjustment of β to a

Table 3
Total and readily-soluble K_2O and Na_2O mass percentages expressed on a total solids basis

Phase	Cement 151		Cement 152	
	Total	Readily soluble	Total	Readily soluble
K_2O	0.320±0.019	0.250	0.500±0.023	0.250
Na_2O	0.269±0.029	0.086	0.191±0.027	0.033

Readily-soluble amounts are equated with concentrations in pore solution after 1 h of curing at 23 °C.

Table 4
Loss on ignition of initial powders and of pastes of cements fully hydrated at room temperature

Cement	Powder (g/g cement)		Fully hydrated (g/g cement)		QXRD
	Normal	Dry	Normal	Dry	
151	0.0108	0.0092	0.2633	0.2018	0.245
152	0.0097	0.0088	0.2686	0.1940	0.238

Values reported are the average of measurements on two different specimens, and the range of the two measurements was no more than 0.1% of the mean value. The final column is the estimate of LOI at full hydration based on quantitative X-ray diffraction analysis of the initial powder.

higher value would yield better agreement with experiments using the 105 °C oven, because the effect of this parameter is to uniformly shift the curves horizontally. However, we choose to keep β constant for a given cement rather than manipulating it simply to give a better appearance of agreement to experimental measurements of any given property.

At either w/c ratio, the measured degrees of hydration are significantly less when the specimens are treated at 105 °C in the dry oven than when they are treated at the same temperature in the normal oven, and the differences increase specimen age. These lower values are expected because of the harsher drying conditions in the dry 105 °C oven. If the 'dry' value for degree of hydration of the fully hydrated cement, shown in Table 4, is used to convert the LOI measurements to degree of hydration, the data using the dry oven lie much more closely to the data acquired using the normal oven.

Fig. 7 shows plots of the model predictions and experimental results for degree of hydration for cement 152 at w/c=0.35 and w/c=0.45. As shown in the figure, a time conversion factor β=0.00020 h/cycle^2 was used at w/c=0.35 and β=0.00030 h/cycle^2 was used at w/c=0.45. As for cement 151, the value of β for cement 152 was fixed at the value of 0.00057 h/cycle^2 determined in Fig. 5. In general, the same trends are observed in Fig. 7 for cement 152 as for cement 151 (Fig. 6), except that the predictions agree somewhat better with the experimental estimates of degree of hydration at both w/c ratios.

3.2. Thermogravimetry

As described earlier, LOI measurements are made by subtracting the mass of a specimen annealed at 1000 °C from the mass of a specimen equilibrated at 105 °C. As Figs. 6 and 7

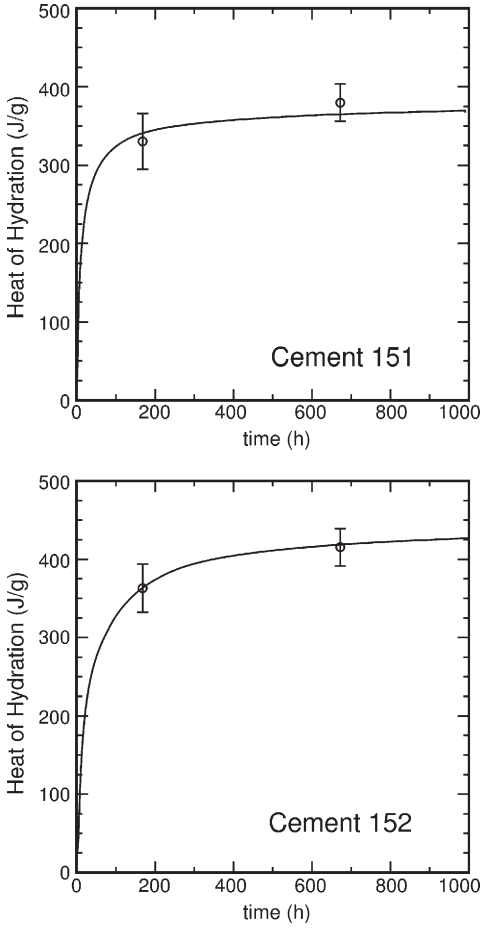

Fig. 5. Computer model (lines) and experimental results (points) for the heat of hydration of cement 151 and cement 152. Error bars represent plus/minus one standard deviation in the values measured by about 20 laboratories. β=0.00020 for cement 151 and β=0.00057 for cement 152.

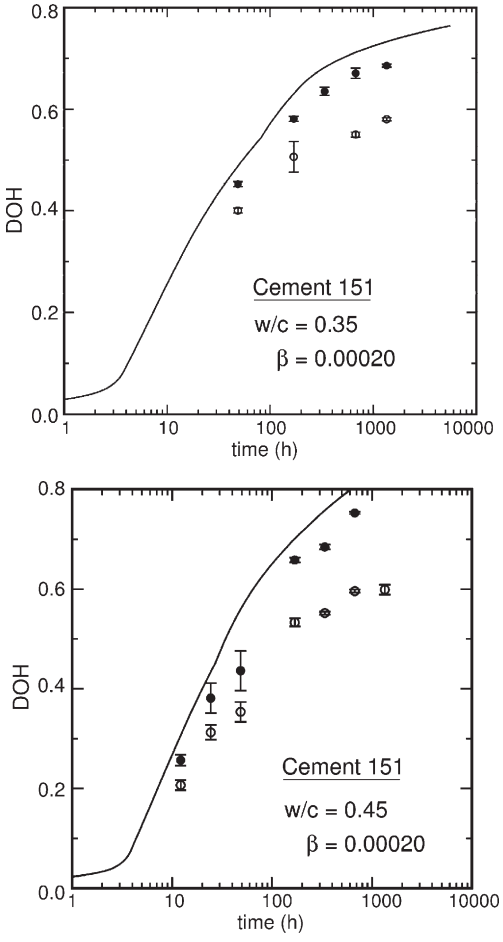

Fig. 6. Computer model (lines) and experimental results (points) for degree of hydration of cement 151 with w/c=0.35 (top) and w/c=0.45, both cured isothermally at 23 °C. Filled circles indicate measurements made with the normal 105 °C oven, and open circles indicate measurements made with the dry 105 °C oven.

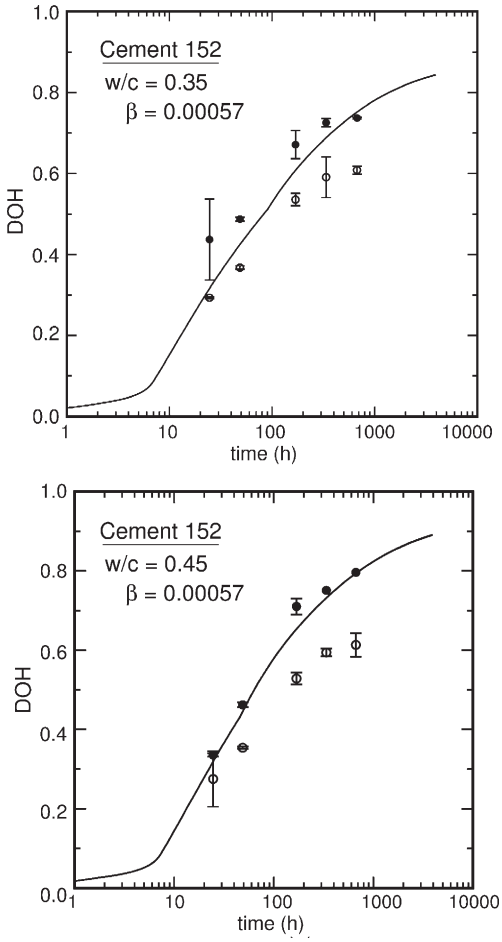

Fig. 7. Computer model (lines) and experimental results (points) for degree of hydration of cement 152 with w/c=0.35 (top) and w/c=0.45.

show, the degree of hydration measured on a paste depends on the moisture and possibly CO_2 content in the atmosphere during the 105 °C treatment. A more detailed examination of the mass loss between 105 °C and 1000 °C was obtained by TGA.

Fig. 8 plots the mass loss as a function of temperature for cement 151 cured at 23 °C to several different hydration ages. The data are plotted in terms of the "rate" of mass change, d*m*/d*T*, where *m* is mass and *T* is temperature. For all these curves, the normal atmosphere was used during the treatment at 105 °C. The main features of this plot are a peak between 450 °C and 550 °C which increases with hydration age, and a smaller peak at about 700 °C which remains roughly the same height with hydration age.

The peak at temperatures between 450 °C and 550 °C is due primarily to dehydration of portlandite, $Ca(OH)_2$, but there also may be some contribution (on the order of 1% of the signal) of AFm dehydration in this range as well [11]. Mass loss above 550 °C are due primarily to decomposition of carbonates although, again, minor contributions due to the final dehydration of C–S–H gel and aluminate phases is also possible.

Fig. 9 shows the influence of the prior heat treatment at 105 °C on the TGA results for the same cement paste shown in Fig. 8. Both at 7 d and 14 d curing time, the small peak at 696 °C, which appears when the normal atmosphere is used at 105 °C, is suppressed when the dry atmosphere is used instead. Recall that

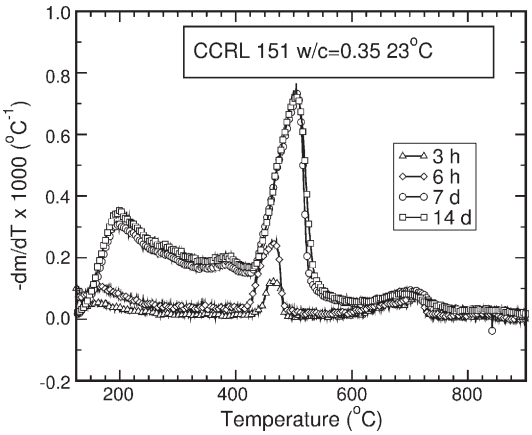

Fig. 8. Differential mass loss as a function of temperature for cement 151 with w/c=0.35, cured at 23 °C to different ages and equilibrated at 105 °C with 'normal' atmospheric conditions.

the latter atmosphere, in addition to having much less moisture content (−70 °C dew point), also is virtually free of CO_2. Any water loss at such high temperatures as even 500 °C must be due to water that is too tightly held to be lost at 105 °C even under dry conditions, as shown by the nearly identical size of the peak at 502 °C in Fig. 9. Therefore, the difference in the curves in that figures imply that the TGA peak at 696 °C is due to carbonation that occurs *during the 105 °C equilibration step*. Although the peak is small in any case, it is a source of error when LOI is used to estimate the degree of hydration.

3.3. Setting time

At least two studies have shown that setting, as measured by the Vicat needle method [2], correlates with the percolation of the solids in 3-D microstructural models of hydration [4,12]. The ASTM method [2] specifies that the initial and final setting times are to be measured on normal consistency (N.C.) pastes. For cements 151 and 152, the N.C. water value measured by the testing laboratories was 25.4 and 26.0, respectively [3]. VCCTL

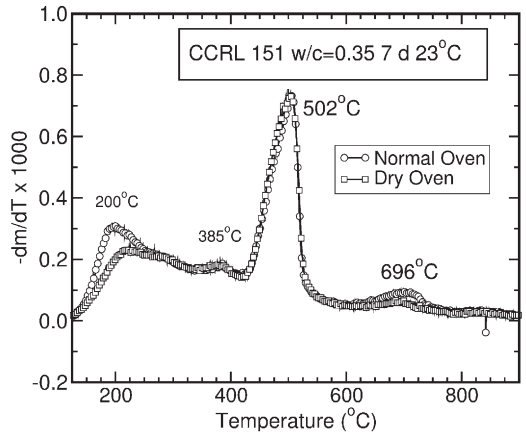

Fig. 9. Differential mass loss as a function of temperature for cement 151 with w/c=0.35, cured at 23 °C. The curve with open circles was obtained after a 105 °C equilibration in ambient laboratory air, and the curve with open squares was obtained after equilibration at the same temperature in dry and CO_2-free air.

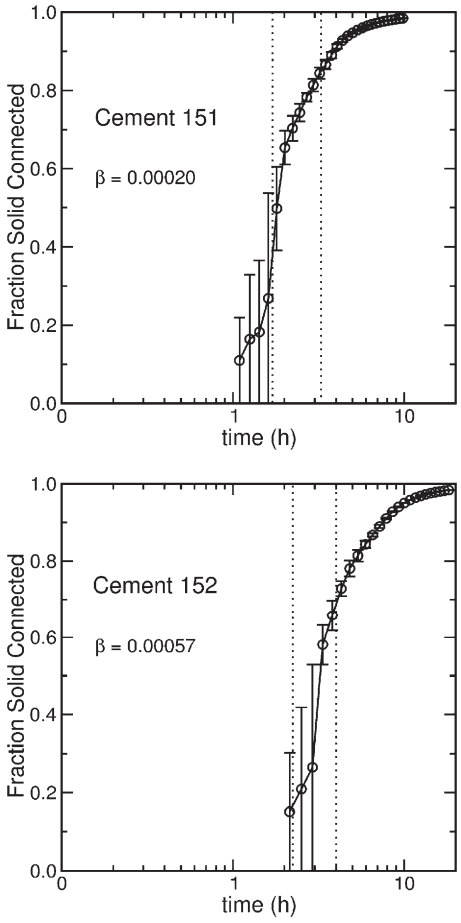

Fig. 10. Volume fraction of connected solids as a function of time predicted by VCCTL for cements 151 (top) and 152. The vertical dashed lines indicate the experimentally measured initial and final setting times as measured by the Vicat needle method.

was used to create 3-D microstructures of cements 151 and 152 with w/c = 0.254 and w/c = 0.260, respectively, and hydration of the microstructures was simulated under conditions like those specified in the Vicat needle method.

Fig. 10 shows the fraction of solids connected as a function of time predicted by for cements 151 and 152. The open circles are predicted values and the error bars indicate the range of values predicted for two statistically identical microstructures. The solid curves are produced to guide the eye. Vertical dashed lines indicate the average experimental values of the initial and final time of set, as measured independently by 159 and 160 laboratories, respectively [3], using the Vicat needle technique described in the ASTM C191 standard test method [2].

The figure indicates that the percolated solid volume fraction gives an approximate indication of the time of set. In a previous study using CEMHYD3D [4], Bentz and coworkers found for CCRL proficiency samples 135 and 141 that solid fractions of 0.40 and 0.75 corresponded well with the initial and final setting times, respectively, measured by the Vicat method. For cements 151 and 152, Fig. 10 indicates that these same values of the percolated solid fraction again provide a reasonable estimate of initial and final set, although the value of 0.40 for initial set seems to be somewhat too high for cement 152.

3.4. Mortar strength development

Simulations of hydration of cements 151 and 152 were performed under conditions close to that specified in the ASTM C109 standard test method for mortar compressive strength [2]. Model cement paste microstructures with w/c = 0.485 were created for both cements 151 and 152, and hydration was simulated with VCCTL at 23 °C under saturated conditions. The predicted and measured compressive strengths for cements 151 and 152 are shown in Fig. 11. Predictions are based on the Powers gel–space ratio correlation between microstructure and compressive strength [11],

$$\sigma = AX^n \tag{3}$$

where σ is the compressive strength, X is the gel–space ratio, and n is an exponent which is assumed to have a fixed value of 2.6, based on prior experience with VCCTL predictions for a number of cements [5,7]. The computer model calculates at each time the value of X for the microstructure, and the prediction of compressive strength is made by calibrating the prefactor A to an experimentally measured compressive strength at 3 d. The time conversion factors used for the predictions in Fig. 11 are again the same as those used in Fig. 5.

Fig. 11 indicates that the strength predictions obtained for cement 151 are in excellent agreement with the measured values at

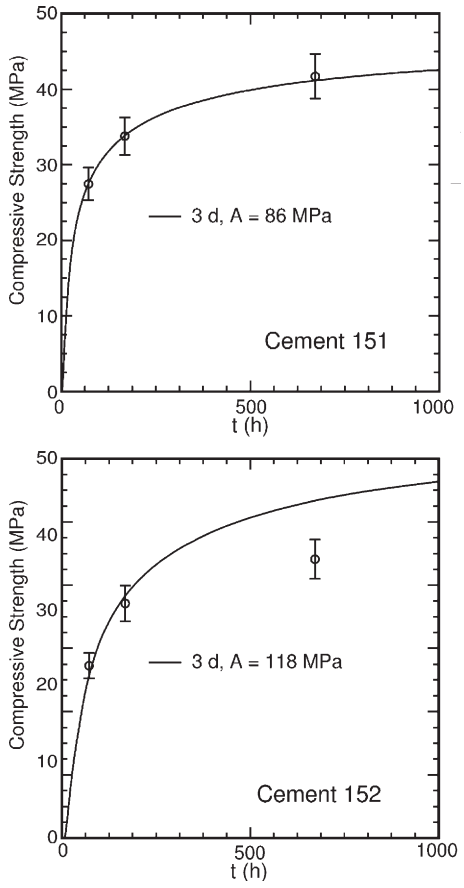

Fig. 11. Computer model (lines) and experimental results (points) for the compressive strength of cement 151 (top) and cement 152.

7 d and at 28 d. In the past, it was observed for CCRL cements 135 and 136 that calibrating to the 7-d measured strength gave a superior fit to all of the experimental data [7], but for cement 151 the fit is so good that it does not matter whether the predictions are calibrated to the 3 d measurement or to the 7 d measurement.

The situation is somewhat different for cement 152. Calibration to the 3 d measurement yields a curve that agrees with the 7 d strength measurement, but which is significantly greater at 28 d than the experimental measurement. The inaccuracy at 28 d is somewhat unexpected because both the heat of hydration at w/c=0.4 (Fig. 5) and the degree of hydration at w/c=0.45 (Fig. 7) were predicted quite well for cement 152 using the same value of the time conversion parameter β. Additional research is required to determine the nature of the later-age deviations in the predicted compressive strengths from the measured values, and to reconcile these deviations to the predictions of the heat of hydration and LOI.

4. Summary

CCRL cements 151 and 152 have been quantitatively characterized based on SEM, X-ray microanalysis, and QXRD. The phase compositions estimated from the SEM images are in close agreement with those measured by QXRD, but they are significantly different from those calculated using the formulas developed by Bogue, which are enumerated in the ASTM C150 specification. Based on the SEM/X-ray analysis, initial three-dimensional cement paste microstructures were created and hydrated using the VCCTL program. Model predictions for degree of hydration, heat of hydration, setting time, and mortar strength development were compared to their experimental counterparts. In most cases, good agreement between model predictions and experimental measurements was obtained. The main exception was the prediction of 28-d compressive strength, which was too high compared to experimentally measured values, especially for cement 152.

Estimates of the degree of hydration using LOI measurements indicated a modest influence of the moisture content and CO_2 levels during equilibration at 105 °C. Specifically, the estimated degree of hydration was significantly lower when a low-moisture, low-CO_2 environment was used at 105 °C than when ambient laboratory air was used. This effect is attributed to the harsher drying conditions which remove a greater mass of water at that temperature. TGA measurements indicated that a modest amount of carbonation of hydration products may occur *during* the treatment at 105 °C when ambient air is used.

Acknowledgments

The authors acknowledge the Virtual Cement and Concrete Testing Laboratory Consortium for partial support of this research. Mr. Dale Bentz provided valuable information about the interpretation of the experimental data, and Mr. Max Peltz provided measurements of the particle size distribution of both cements.

References

[1] D.P. Bentz, P.E. Stutzman, C.J. Haecker, S. Remond, SEM/X-ray imaging of cement-based materials, in: H.S. Pietersen, J.A. Larbia, H.H.A. Janssen (Eds.), Proceedings of the 7th Euroseminar on Microscopy Applied to building Materials, Delft University of Technology, 1999, pp. 457–466.
[2] Annual Book of ASTM Standards, vol. 04.01, American Society for Testing and Materials, West Conshohocken, PA, 2000.
[3] Final Report: Portland Cement Proficiency Samples Number 151 and Number 152, Cement and Concrete Reference Laboratory, 2004.
[4] C.J. Haecker, D.P. Bentz, X.P. Feng, P.E. Stutzman, Prediction of cement physical properties by virtual testing, Cem. Int. 1 (3) (2003) 86–92.
[5] D.P. Bentz, Three-dimensional computer simulation of cement hydration and microstructure development, J. Am. Ceram. Soc. 80 (1) (1997) 3–21.
[6] D.P. Bentz, CEMHYD3D: a three-dimensional cement hydration and microstructural development modelling package. version 2.0, NISTIR, vol. 6485, U.S. Department of Commerce, 2000.
[7] D.P. Bentz, X. Feng, C.J. Haecker, P.E. Stutzman, Analysis of CCRL proficiency cements 135 and 136 using CEMHYD3D, NISTIR, vol. 6545, U.S. Department of Commerce, 2000.
[8] J.W. Bullard, P.E. Stutzman, "Analysis of CCRL Proficiency Cements 151 and 152 Using the Virtual Cement and Concrete Testing Laboratory" NIST IR In review 2005.
[9] D.P. Bentz, P.E. Stutzman, SEM analysis and computer modelling of hydration of portland cement particles, in: S.M. DeHayes, D. Stark (Eds.), Petrography of Cementitious Materials, American Society for Testing and Materials, Philadelphia, PA, 1994, pp. 60–73.
[10] K.R. Castleman, Digital Image Processing, Prentice-Hall, Englewood Cliffs, NJ, 1979.
[11] H.F.W. Taylor, Cement Chemistry, 2nd edition, Thomas Telford, London, 1997.
[12] Princigallo, P. Lura, K. van Breugel, G. Levita, Early development of properties in a cement paste: a numerical and experimental study, Cem. Concr. Res. 33 (7) (2003) 1013–1020.